NOVEL WALL-MOUNTED HOT-FILM SENSORS FOR THE MEASUREMENT OF THE FORCED CONVECTION FROM AN OPEN CYLINDRICAL CAVITY

Silvan Siegrist*, Hannes Stadler
Institute of Solar Research, German Aerospace Center (DLR), Prof.-Rehm-Str. 1, 52428 Juelich, Germany
*silvan.siegrist@dlr.de
Bernhard Hoffschmidt
Institute of Solar Research, German Aerospace Center (DLR), Linder Hoehe, 51147 Koeln, Germany

Abstract. We investigated the forced convective heat loss from a model of a multi-MW cavity receiver of a concentrated solar power (CSP) tower system in a high-pressure wind tunnel. For the tests, arrays of a novel ringlike design of hot-film sensors were placed on the inside wall of the open cylindrical cavity. A constant temperature anemometry (CTA) system controlled these sensors and returned a signal as a function of the instantaneous total heat loss in each sensor. This heat loss was interpolated and averaged to form an integral heat loss value for each given set of wind speed and wind direction. The experiments covered a Reynolds number range of between $2 \cdot 10^6$ and $8 \cdot 10^6$, based on the external flow field. During the 10 days of testing, the ringlike hot-film sensors worked reliably and proved to deliver significant and reproducible results. The maximum forced convective heat loss for the tested geometry occurs at an incident angle of 70°, at all tested Reynolds numbers.

Keywords: hot-film sensor, constant temperature anemometry, forced convection, high-pressure wind tunnel, concentrated solar power cavity receiver

1. INTRODUCTION

During the operation of multi-MW receivers of concentrated solar power (CSP) tower systems, heat is lost mainly due to (a) the partial reflection of the incoming solar radiation on the receiver surface, (b) the radiation from the hot receiver surfaces to the surroundings, (c) the conduction to support structures and (d) the mixed convection from the hot receiver surfaces to the surroundings.

In previous research, it has been shown that the local wind speed has a significant influence on the convective heat loss. See Flesch *et al.* (2015) for a recent summary of the state of knowledge concerning convective heat loss from CSP cavity receivers. Though there have been many studies concerning the convective heat loss, the convective heat loss on multi-MW scale remains difficult to measure on original scale due to the complicated geometries and large dimensions of such receivers. Further, one expects Reynolds numbers Re of up to 10^7 and Grashof numbers Gr of up to 10^{14}. Thus, a physically similar modeling on smaller length scales is hardly feasible if one would like to model the mixed convection and thus would need to keep both dimensionless numbers constant. For this reason, we chose to measure only the forced convection in this study and therefore, only the Reynolds similarity needs to be adhered to.

Hot-film sensors controlled by a constant temperature anemometry (CTA) system measure the voltage needed to keep the sensors at a predefined temperature. In conventional CTA measurements this voltage is correlated to velocity or to wall shear stress via calibration and empirical functions. A good overview on hot-film and hot-wire anemometry is given by Comte-Bellot (1976), Lomas (1986), and Tropea *et al.* (2007). In our study, we used the output voltage of wall-mounted hot-film sensors directly to calculate the heat loss. Conventional hot-film sensors are most often produced in straight form which causes the measured value to depend strongly on the incident angle, see e.g. Lomas (1986) or Tropea *et al.* (2007). To overcome this drawback multiple straight sensors are commonly used in different geometrical arrangements. In this context, the reader is referred to the work by McCroskey and Durbin (1972), and Sumer *et al.* (1993). If the information of the flow direction is not needed this means unnecessary additional costs for signal controlling and processing due to the increased number of sensors. Hereafter, we introduce a sensor design which is as independent of the direction as technically possible.

2. EXPERIMENTAL METHODS

2.1 Experimental setup

The investigation was carried out in the high-pressure wind tunnel (HDG) in Goettingen. This wind tunnel operates at pressures from ambient up to 10 MPa and at ambient temperatures. The achievable wind speeds are between approximately 3.5 and 35 m/s. The test section has a cross-section of 0.6 m by 0.6 m. All experiments of this study were carried

out at a pressure of 6 MPa and at temperatures between 293 K and 305 K. The setup was designed in order to have a flow regime dominated by forced convection, which is true if Eq. (1) holds.

$$\frac{Gr}{Re^2} << 1 \tag{1}$$

In our setup, a low overheat ratio of the sensors and small characteristic length scales were combined with higher wind speeds (but still satisfying $Ma < 0.1$) and a high density. The most conservative estimation of this ratio for this experiment is obtained by assuming a uniformly heated inside at sensor temperature and the lowest Reynolds number. The result of this estimation is $Gr/Re^2 < 2 \cdot 10^{-3}$.

The model was built modularly in order to easily change the geometry. The selected model geometry represents approximately the upper half of a simplified CSP tower system with a cavity receiver in the order of 100 MW thermal output power. The length scale of the model was 1:250. The part that is exposed to the flow in the wind tunnel test section was 0.4 m high and had a diameter of 0.08 m, see Fig. 1. From the exposed part, the lowest 0.05 m were tapered and shielded by a thin cylinder of 0.08 m diameter which had no contact with the model in order to minimize the influence of the boundary layer of the wind tunnel on the measurements. The cavity had an inner diameter $d_{\mathrm{cav,in}}$ of 0.06 m and a length-to-diameter ratio $l_{\mathrm{cav,in}}/d_{\mathrm{cav,in}}$ of 1. An aperture-to-inner-diameter ratio $d_{\mathrm{cav,ap}}/d_{\mathrm{cav,in}}$ of 0.8 was chosen. The cavity faced the horizontal, thus $\gamma = 0°$. The whole model was mounted on a force balance on a rotary table in the wind tunnel test section. The measurements were taken at $Re = [2 \cdot 10^6, 4 \cdot 10^6, 6 \cdot 10^6, 8 \cdot 10^6]$ in steps of the incident angle α of 10° from 0° to 180°. For data correction purposes, an additional measurement at 0° is taken after the completion of the incident angle series as well as measurements without wind before and after each test series were taken.

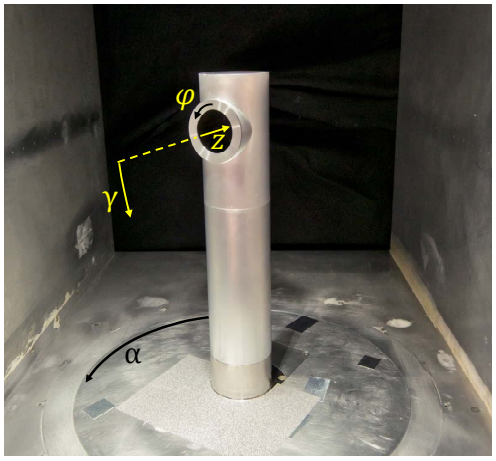

Figure 1. Wind tunnel model with $\gamma = 0°$ mounted on a rotary table in the test section. φ and z define the inner surface of the cavity, γ the cavity inclination and α the wind incident angle.

2.1.1 Ringlike wall-mounted hot-film sensors

Since conventional, straight hot-film sensors are highly sensitive to the flow direction (see Lomas (1986)), novel sensors were designed. From symmetrical considerations follows, that one could obtain a perfect flow direction independence for a closed ring sensor. But, since the sensor needs two leads for the connection to the anemometry system, it is not possible to perfectly close the ring. And hence, the perfect shape was approximated by a ringlike sensor, as shown in Fig. 2. The sensor angle ω spanned more than 5/6 of a full circle.

Having a more direction independent sensor is beneficial for flow measurements when the main flow direction is unknown or of no interest and if only the magnitude of the wall shear stress or convective heat loss is of interest. Therefore, we expect that this sensor design is more adequate for complex flows such as in open cavities.

After production, the sensors had a resistance in the range 9.1 Ω to 9.7 Ω. The sensor material was nickel and the lead material was copper. The sensors were produced on a polyimide film which was then glued on the inside of the cavity to a base of 2 mm thick polyoxymethylene (POM). The cavity was placed at the top of the model, as shown in Fig. 1. To have a good spatial resolution and some redundancy in case of broken sensors, a total of 32 sensors were placed in a regular pattern which is shown in cylindrical coordinates φ and z in Fig. 3. Of the 32 sensors, 8 were unusable right after the installation, mainly due to installation and fabrication problems related to the limited and complicated space inside the wind tunnel model. During operation no more sensors broke. The location of the working and broken sensors can be seen in Fig. 3.

The sensor leads are led through slits in the back of the cavity. The slits were sealed with isolating epoxy resin to close the back of the cavity. Figure 4 shows the mounted sensor arrays in the cavity. On the outside of the back of the cavity,

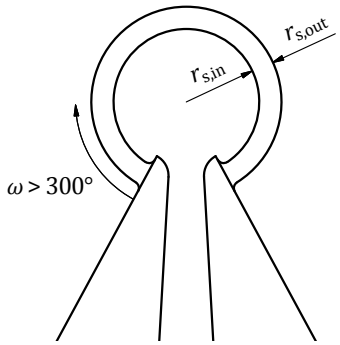

Figure 2. Ringlike hot-film sensor design. The sensor spanned more than 300°. $r_{\mathrm{s,in}}$ and $r_{\mathrm{s,out}}$ are the inner and outer radius of the sensor, respectively. The tapered objects reaching from below are the two leads.

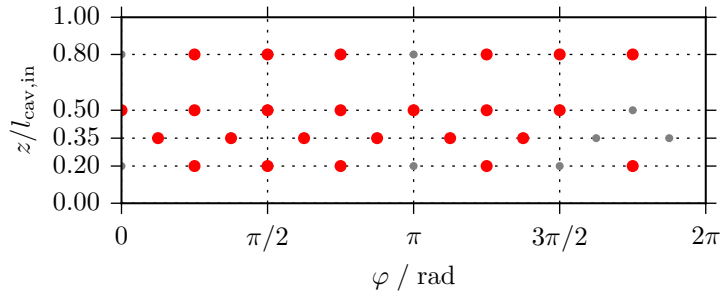

Figure 3. Sensor pattern on the inside of the cavity. φ and z define the inner surface of the cavity. Red, large markers symbolize working sensors and grey, small markers symbolize broken sensors.

which is still inside the tower, the sensor leads were soldered to shielded twisted pair wires until the air lock door. From there, a standard coaxial cable was used to connect to the CTA system.

Figure 4. 32 sensors were placed inside the cavity in a regular pattern. They sit at the visible end of the thick coppery leads of the sensors, which are leading out through thin slits in the back of the cavity.

An in-house CTA system was used to adjust and control the sensor heating. The absolute temperature of each sensor was adjusted in the beginning of each test day and has then been kept constant during the following test series. After adjustment of the CTA system, the system including the sensors reached a maximum cut-off frequency of around 35 kHz.

At each measurement point, the output voltage of the CTA system was sampled for 30 s with a sample rate of 10 kHz. Expected flow frequencies, e.g. due to vortex shedding, were expected to be in the order of 100 Hz. Thus, the sample rate is well above the Nyquist rate.

2.1.2 Temperature coefficient of resistance

In Eq. (5) and Eq. (7) of the next section, it is shown that one needs to know the exact temperature of each sensor in order to calculate absolute heat loss values. Assuming a linear approach, Lomas (1986) describes the variation of the resistance with temperature as follows

$$R(T_\mathrm{w}) = R(T_\mathrm{ref})(1 + \alpha_0(T_\mathrm{w} - T_\mathrm{ref})) \tag{2}$$

with R being the resistance of a sensor, T_w the temperature of a hot sensor, T_ref the reference temperature of a cold sensor and α_0 the temperature coefficient of resistance of the sensor material. Under operation, both resistances are known. Thus, it is only necessary to additionally know the temperature coefficient of resistance to compute the temperature difference. The values of α_0 were determined by a separate measurement with the actual sensors after the wind tunnel tests. All sensors were placed in a drying cabinet. The temperature was raised in steps of maximum 5 K from 297 K up to 333 K. Once thermal equilibrium was reached at each step, the resistances were measured. Thereafter, the data was fitted for each sensor by a linear regression to obtain α_0 for each sensor. In Table 1 the resulting temperature coefficients of resistance are listed together with their corresponding sensor positions.

Table 1. Measured temperature coefficient of resistance for each of the working sensors.

Sensor position		Temperature coefficient of resistance
φ / °	z / $l_\mathrm{cav,in}$	α_0 / 10^{-3} K^{-1}
0	0.5	3.645
22.5	0.35	3.163
45	0.2	3.578
45	0.5	3.538
45	0.8	3.578
67.5	0.35	3.408
90	0.2	3.421
90	0.5	2.919
90	0.8	3.424
112.5	0.35	3.178
135	0.2	3.289
135	0.5	3.175
135.0	0.8	2.832
157.5	0.35	2.765
180.0	0.5	3.110
202.5	0.35	3.084
225.0	0.2	3.230
225.0	0.5	3.317
225.0	0.8	3.239
247.5	0.35	3.565
270.0	0.5	2.634
270.0	0.8	3.272
315.0	0.2	3.417
315.0	0.8	3.300
Median		3.281

2.2 Data processing

Since all resistances are known, the voltage drop across a sensor E_s can be calculated from the measured output (bridge) voltage of the CTA system. Then, the heat dissipated in a sensor $\dot{Q}_\mathrm{s}$ equals the electrical power of a sensor $P_\mathrm{el,s}$ which is a function of the sensor voltage and the sensor resistance at operating temperature R_w, see Lomas (1986).

$$\dot{Q}_\mathrm{s} = P_\mathrm{el,s} = \frac{E_\mathrm{s}^2}{R(T_\mathrm{w})} = \dot{Q}_\mathrm{conv,forc,s} + \dot{Q}_\mathrm{conv,free,s} + \dot{Q}_\mathrm{rad,s} + \dot{Q}_\mathrm{cond\rightarrow supp,s} + \dot{Q}_\mathrm{cond\rightarrow lead,s} \tag{3}$$

Under no-wind conditions, this power is the sum of the convective heat loss due to free convection $\dot{Q}_{\mathrm{conv,free,s}}$, the radiative heat loss $\dot{Q}_{\mathrm{rad,s}}$, the conductive heat loss to the support material $\dot{Q}_{\mathrm{cond\rightarrow supp,s}}$ and the conductive heat loss to the leads $\dot{Q}_{\mathrm{cond\rightarrow lead,s}}$. The latter three remain constant for a constant sensor temperature and under steady state operation. With wind, additional loss occurs only due to forced convection. Therefore, the forced convective heat loss $\dot{Q}_{\mathrm{conv,forc,s}}$ can be obtained by taking the difference of the power at a measurement point with wind $P_{\mathrm{el,s,wind}}$ and the power without wind $P_{\mathrm{el,s,calm}}$. This results in the additional power $\Delta P_{\mathrm{el,s}}$ needed to keep a sensor at the desired temperature with wind.

$$\Delta P_{\mathrm{el,s}} = P_{\mathrm{el,s,wind}} - P_{\mathrm{el,s,calm}} = \dot{Q}_{\mathrm{conv,forc,s}} \tag{4}$$

Combining Eq. (4) with the equation for the forced convective heat transfer and with the definition of the Nusselt number Nu

$$\dot{Q}_{\mathrm{conv,forc,s}} = h_{\mathrm{s}} A_{\mathrm{s}} \Delta T = h_{\mathrm{s}} A_{\mathrm{s}} (T_{\mathrm{w}} - T_{\infty}) \tag{5}$$

$$Nu = \frac{h_{\mathrm{s}} L_{\mathrm{s}}}{k_{\mathrm{air}}} \tag{6}$$

we obtain the following alternative expression for the Nusselt number

$$Nu = \frac{4}{\omega} \frac{\Delta P_{\mathrm{el,s}} r_{\mathrm{s,out}}}{k_{\mathrm{air}} (r_{\mathrm{s,out}}^2 - r_{\mathrm{s,in}}^2) \Delta T} = C_{\mathrm{s}} \frac{\Delta P_{\mathrm{el,s}}}{k_{\mathrm{air}} \Delta T} \tag{7}$$

with h_{s} being the heat transfer coefficient, A_{s} the sensor surface area, ΔT the temperature difference between sensor operating temperature T_{w} and fluid temperature T_{∞}, $L_{\mathrm{s}} = 2r_{\mathrm{s,out}}$ the characteristic length of the sensor, k_{air} the thermal conductivity of air at fluid temperature and $r_{\mathrm{s,out}}$ and $r_{\mathrm{s,in}}$ the outer and inner radius of the sensor, respectively. We combine all the geometrical parameters of a sensor into a sensor shape constant C_{s} in order to enhance the readability of the formula.

The Nusselt number from Eq. (7) for a sensor can then be interpolated on and integrated over the whole surface to obtain an integral value for the heat loss at each set of measurement parameters. For the interpolation a 2D cubic interpolation scheme was chosen. The forced convective heat loss at the front and at the back are set to zero because theory states that the wall shear stress is zero in corners and that the wall shear stress is related to the convective heat loss via the Reynolds analogy, see e.g. Kakac *et al.* (2014).

The representation of measured data by the Nusselt number is convenient, because it already incorporates temperature changes of the fluid during measurements. Thus, a separate correction for fluid temperature changes becomes obsolete.

3. RESULTS

The aforementioned interpolation of the Nusselt number is shown exemplary in Fig. 5 for a horizontal cavity, an incident angle of 70° and a Reynolds number of $8 \cdot 10^6$.

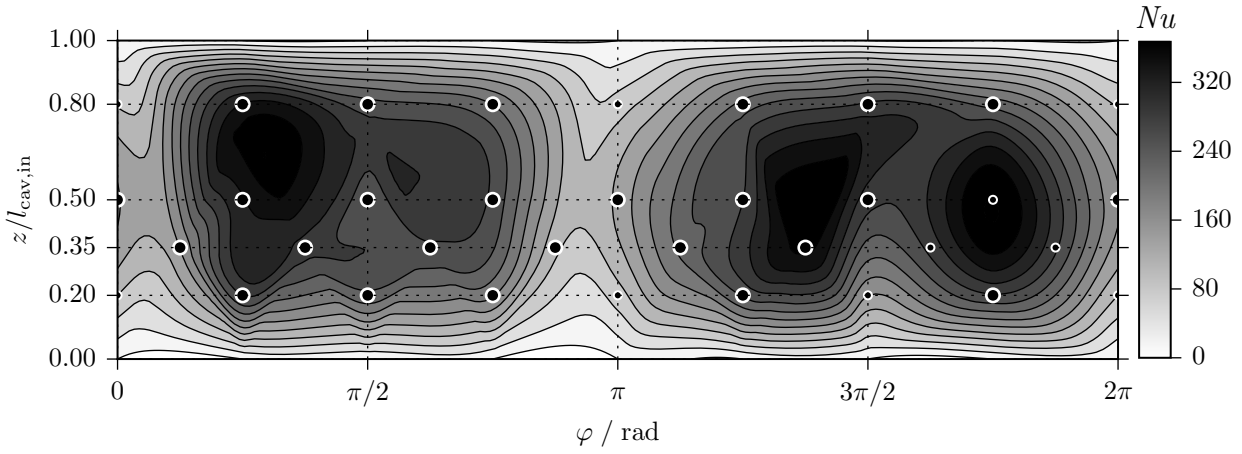

Figure 5. Contour plot of the interpolated Nusselt number based on the forced convective heat loss from the cylindrical inside of the cavity for $\alpha = 70^{\circ}$, $\gamma = 0^{\circ}$ and $Re = 8 \cdot 10^6$. Large markers symbolize the working sensors and small markers the broken sensors.

The graph shows two larger regions of higher heat loss, namely at around $3\pi/2$ and $\pi/2$. The former is on the inside of the cavity where the wind hits the surface directly at this incident angle, the latter is on the opposite side. The right side

maximum at $3\pi/2$ shows a double peak with an angular distance of about $3\pi/8$. Both, the gradients' steepness and the peaks' locations are shifted against the direction of the flow. On the right side this means in negative z direction, on the left side it means in positive z direction. Finally, one can also observe two minima at 0 and π which are located at the top and at the bottom of the cavity inside, respectively.

Figure 6 shows the ratio of the integrated Nusselt numbers to the overall maximum integrated Nusselt number, both based on the forced convection, for a horizontal cavity. It shows a steep increase of the relative heat loss with increasing incident angle at all Reynolds numbers. At $50°$ and $60°$, an intermediate plateau occurs. Then, the heat loss continues to rise to a clear maximum located at an angle of $70°$. The maximum is located at the same incident angle at all the Reynolds numbers. After the peak, the values fall steeply until a plateau is reached for each Reynolds number when the wind blows from a perpendicular angle. The level of each plateau is close to the level at head-on situation. After $150°$, the test series show additional maxima for a downstream facing cavity, but only for Reynolds numbers of $4 \cdot 10^6$ and higher. At the lowest Reynolds number, the convective heat loss even becomes lower.

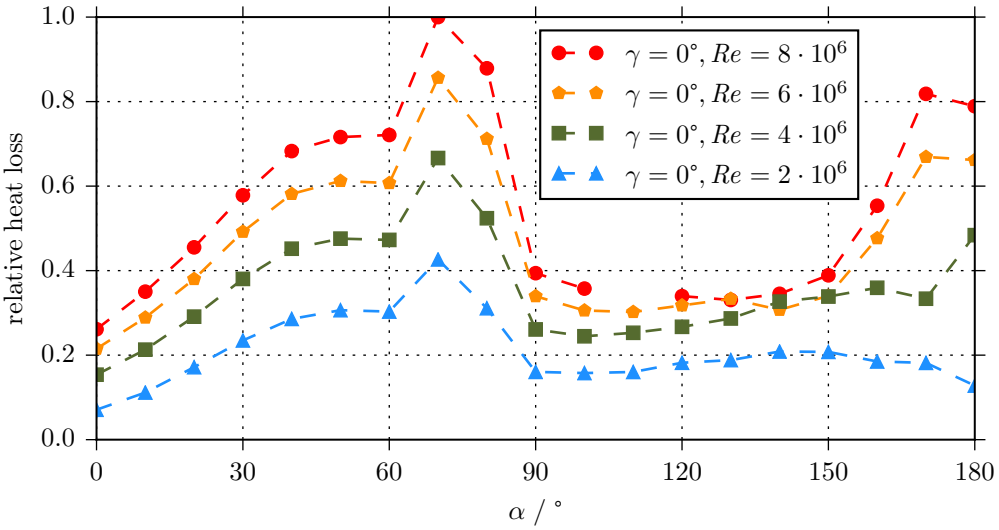

Figure 6. Relative forced convective heat loss for a horizontal cavity ($\gamma = 0°$) and for 4 Re series. Each series was measured at steps of α of $10°$. One missing point due to force balance restrictions at $[Re = 8 \cdot 10^6, \alpha = 110°]$.

As expected, the relative heat loss increases with higher Reynolds numbers. Except for a few angles between $130°$ and $150°$ at the three highest Reynolds numbers, this effect was observed throughout all test series.

In order not to damage the force balance, some measurement points could not be measured. In the presented results, that was only a single point at $[Re = 8 \cdot 10^6, \alpha = 110°]$.

4. DISCUSSION AND CONCLUSIONS

As anticipated the interpolated Nusselt numbers in Fig. 5 show two local maxima at the right and at the left inside of the cavity and two local minima at the top and at the bottom in the cavity. This can be explained by the speed of the fluid which is highest around the point of direct impingement and lowest at the axis of rotation of the main eddy in the cavity. Concluding from this data, we expect a recirculating flow inside the cavity. Although some of the sensors were broken, we could still perform a meaningful interpolation of the data. The drawback of the point-wise measurement of the forced convective heat loss is that absolute Nusselt numbers should be treated with caution. Due to the discrete heating of the surface, the thermal boundary layer is not the same as for an all-heated surface. This is expected to overestimate the absolute levels of the measured heat loss.

The increase of the forced convective heat transfer in all data series up to $\alpha = 70°$, lets us conclude that the fluid exchange with the surroundings increases with the incident angle from head-on to lateral directions. In a previous study, Flesch *et al.* (2015) measured the mixed convection from a simple cavity without tower, the maximum of this exchange occurred at $90°$. One of the reasons for this difference might be the examination of only the forced convection in our study. Another possible cause why it occurred at smaller incident angles can be the presence of the supporting tower. Due to the deflection of the flow at the tower towards the aperture of the cavity, the flow in front of the aperture becomes parallel to the aperture at smaller incident angles. As soon as the flow is parallel, the heat loss is reduced significantly. An additional reason can be the effect of vortex generation at the upstream edge of the aperture at angles around $70°$. This additional amount of turbulence can then augment the exchange of fluid across the aperture.

Between $90°$ and $150°$, the geometry of the tower-cavity ensemble disturbs the flow enough to produce a large wake

zone, wherein the cavity aperture then lies. Since the geometry is strongly asymmetric and contains sharp edges, it will cause the flow to detach at these sharp edges. The so-caused wake zone is relatively quiet, and therefore the exchange of fluid and thus also the exchange of heat from the inside of the cavity to the surroundings is relatively low. Once the sharp edges enter the wake of the tower, the geometrical symmetry is becoming more intact. As a consequence, the wake is coming closer to the tower. In turn, this could ease the propagation of fluctuations from the wake to the inside of the cavity and hence more fluid and heat are exchanged from the insides to the surroundings.

The new sensors were successfully operated for a test period of 10 full days at 6 MPa and up to 35 m/s. The measurement of a single Reynolds number series was fast and took about 0.5 h. Repeated measurements of the same configuration produced the same qualitative and quantitative behavior of the data.

We conclude that the presented method of measuring the forced convection from the inside of a cavity by means of a ringlike hot-film sensor design delivers significant and reproducible results. Obtained data can be interpreted meaningfully. The method is also suitable to obtain highly resolved spatial and temporal data. It is an adequate technique to measure the forced convection from complicated geometries and confined spaces. The new sensors can also be integrated in existing anemometry systems very easily. And in case a wide range of experimental parameters are investigated, this method enables to measure the range quickly.

The analysis of all geometrical configurations which have been measured in this campaign is ongoing. Especially, the comparison of the different configurations will be tackled with the aim to reduce the convective heat loss from future CSP tower systems by improved design. In addition, an uncertainty analysis will be added to the measured data. To further enhance the understanding of the convective heat loss from large cavity receivers, a subsequent numerical study on the natural and mixed convection effects will be performed for the same geometry.

5. ACKNOWLEDGEMENTS

We want to thank (in alphabetic order) Andreas Benkel, Arne Tiddens, Karsten Steiner, Markus Jacobs, Markus Loehr, Matthias Offergeld, Nils van Hinsberg, Robert Flesch, and Stefan Koch for fruitful discussions and valuable support during the experiments.

This work was carried out with financial support from the Ministry of Innovation, Science and Research of the State of North Rhine-Westphalia (MIWF NRW), Germany under contract 323-2010-006 (Start-SF).

6. REFERENCES

Comte-Bellot, G., 1976. “Hot-wire anemometry”. *Annual Review of Fluid Mechanics*, Vol. 8, pp. 209–231.

Flesch, R., Stadler, H., Uhlig, R. and Hoffschmidt, B., 2015. “On the influence of wind on cavity receivers for solar power towers: An experimental analysis”. *Applied Thermal Engineering*, Vol. 87, pp. 724–735.

Kakac, S., Yener, Y. and Pramuanjaroenkij, A., 2014. *Convective Heat Transfer*. CRC Press, Boca Raton, 3rd edition.

Lomas, C.G., 1986. *Fundamentals of Hot Wire Anemometry*. Cambridge University Press, Cambridge, 1st edition.

McCroskey, W.J. and Durbin, E.J., 1972. “Flow angle and shear stress measurements using heated films and wires”. *Journal of Basic Engineering*, Vol. 94, pp. 46–52.

Sumer, B.M., Arnskov, M.M., Christiansen, N. and Jorgensen, F.E., 1993. “Two-component hot-film probe for measurements of wall shear stress”. *Experiments in Fluids*, Vol. 15, pp. 380–384.

Tropea, C., Yarin, A. and Foss, J.F., 2007. *Springer Handbook of Experimental Fluid Mechanics*. Springer, Berlin, 1st edition.